nature portfolio

https://doi.org/10.1038/s41588-022-01061-8

Supplementary information

Meningioma DNA methylation groups identify biological drivers and therapeutic vulnerabilities

In the format provided by the authors and unedited

Supplementary figures and legends

Supplementary figure 1. Clinical outcomes across meningioma DNA methylation discovery and validation cohorts.

a, Kaplan-Meier curves for meningioma local freedom from recurrence (n=565) across clinical contexts (Log-rank tests). **b**, Kaplan-Meier curves for meningioma overall survival (n=565) across clinical contexts (Log-rank tests).

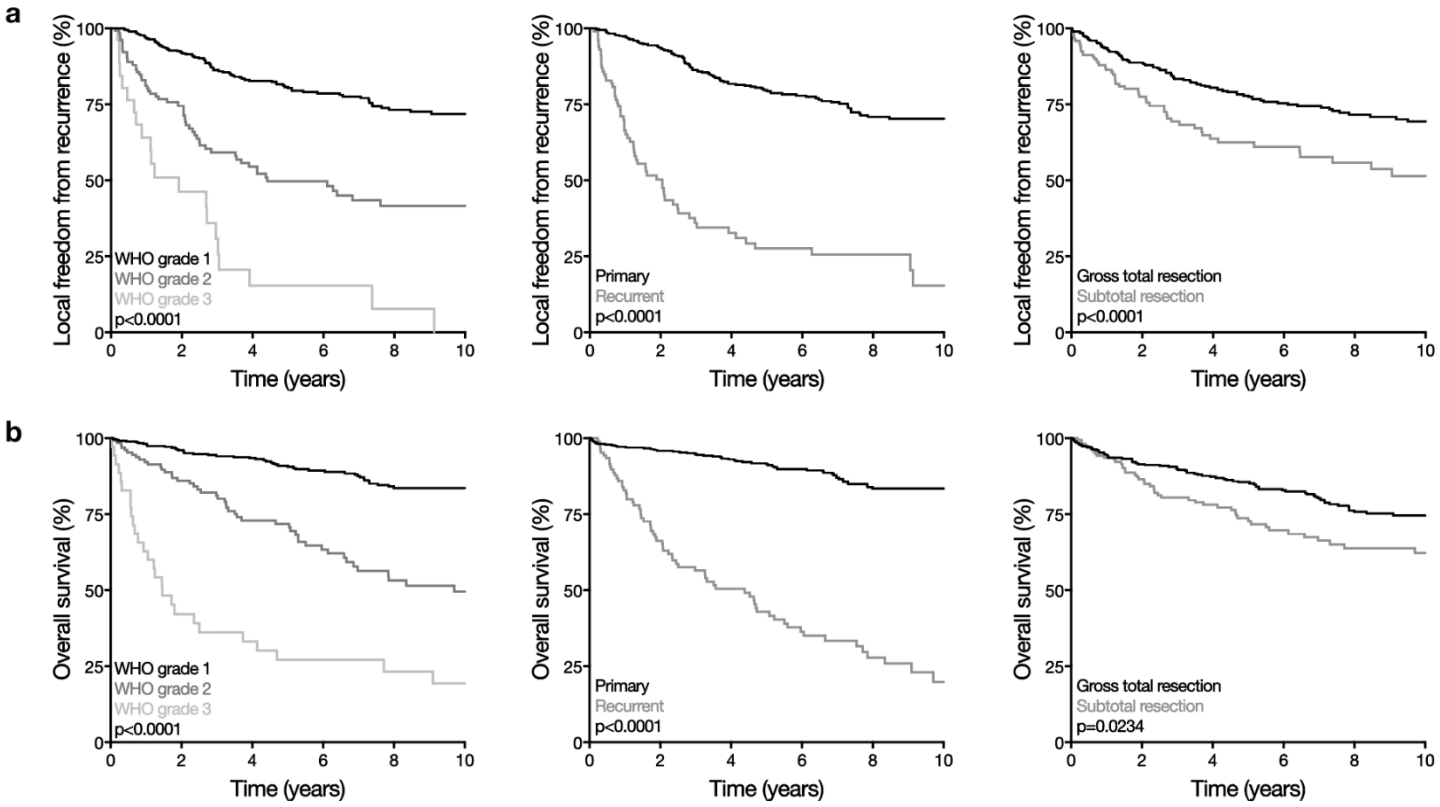

Supplementary figure 2. Clinical correlations across meningioma DNA methylation groups.
a, Kaplan-Meier curve for overall survival (n=565) across meningioma DNA methylation groups (Log-rank test). **b**, Meningioma clinical features (n=565) across DNA methylation groups (Chi-squared tests, two-sided). GTR, gross total resection. STR, subtotal resection. **c, d**, Kaplan-Meier curves for meningioma local freedom from recurrence (n=565) across WHO grades and DNA methylation groups (Log-rank tests). **e**, Multivariable regression hazard ratio (HR) forest plots for overall survival using meningioma clinical variables and DNA methylation groups (n=565, Cox proportional hazards model, Wald test, two-sided, no adjustment for multiple comparisons). Age per year older than the median. Boxes represent means, and error bars represent 95% confidence intervals (CI).

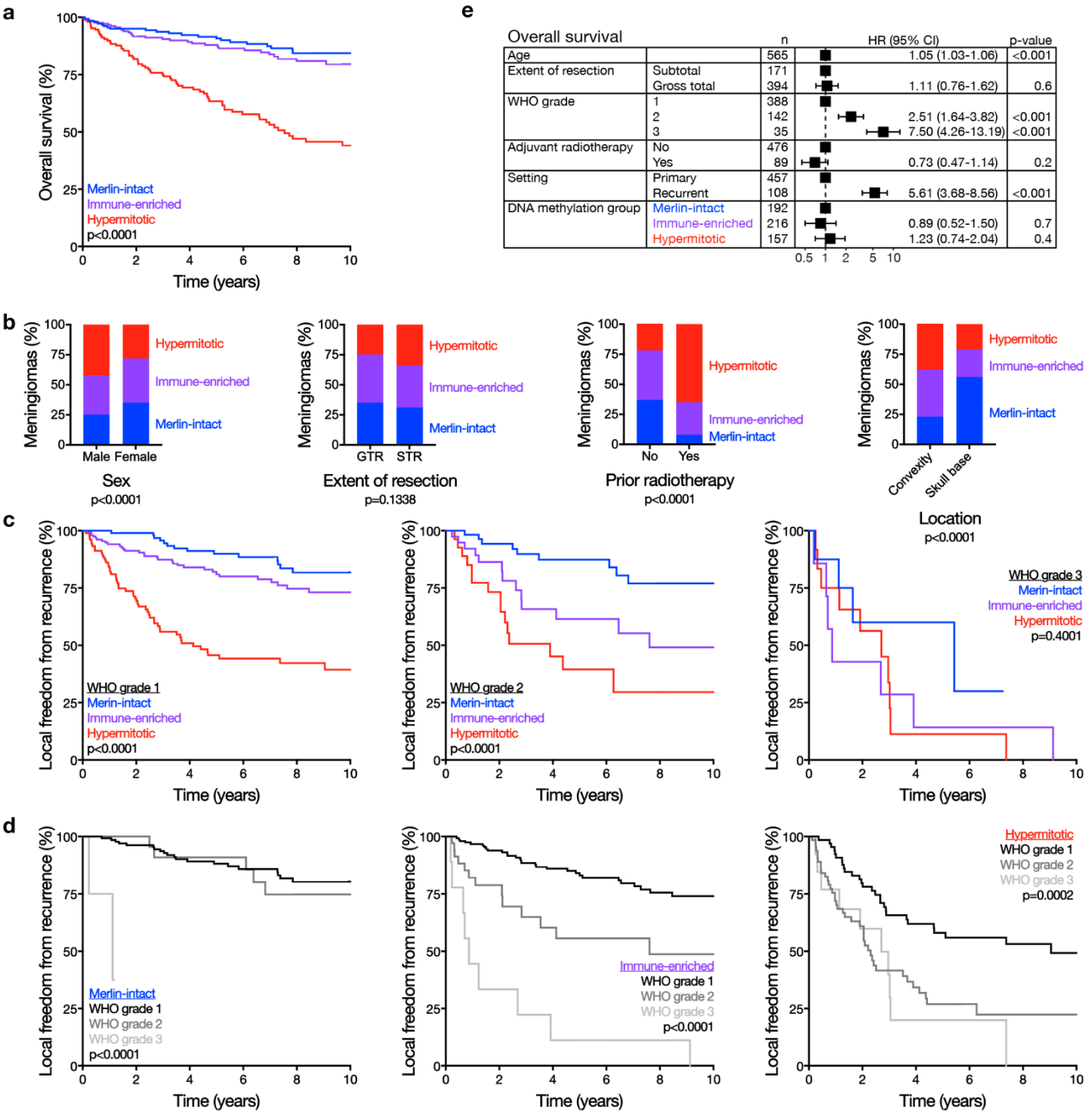

Supplementary figure 3. CNVs across meningioma DNA methylation groups.
a, Frequency of copy number losses (blue) and gains (red) across meningioma DNA methylation groups. **b**, Meningioma genomes (n=565) with copy number variations (CNVs) across DNA methylation groups (ANOVA, one-sided). Lines represent means, and error bars represent standard error of the means. **c**, Analysis of meningioma pairs with overlapping CNVs reveals 37% of meningiomas with identical CNVs are assigned to different DNA methylation groups.

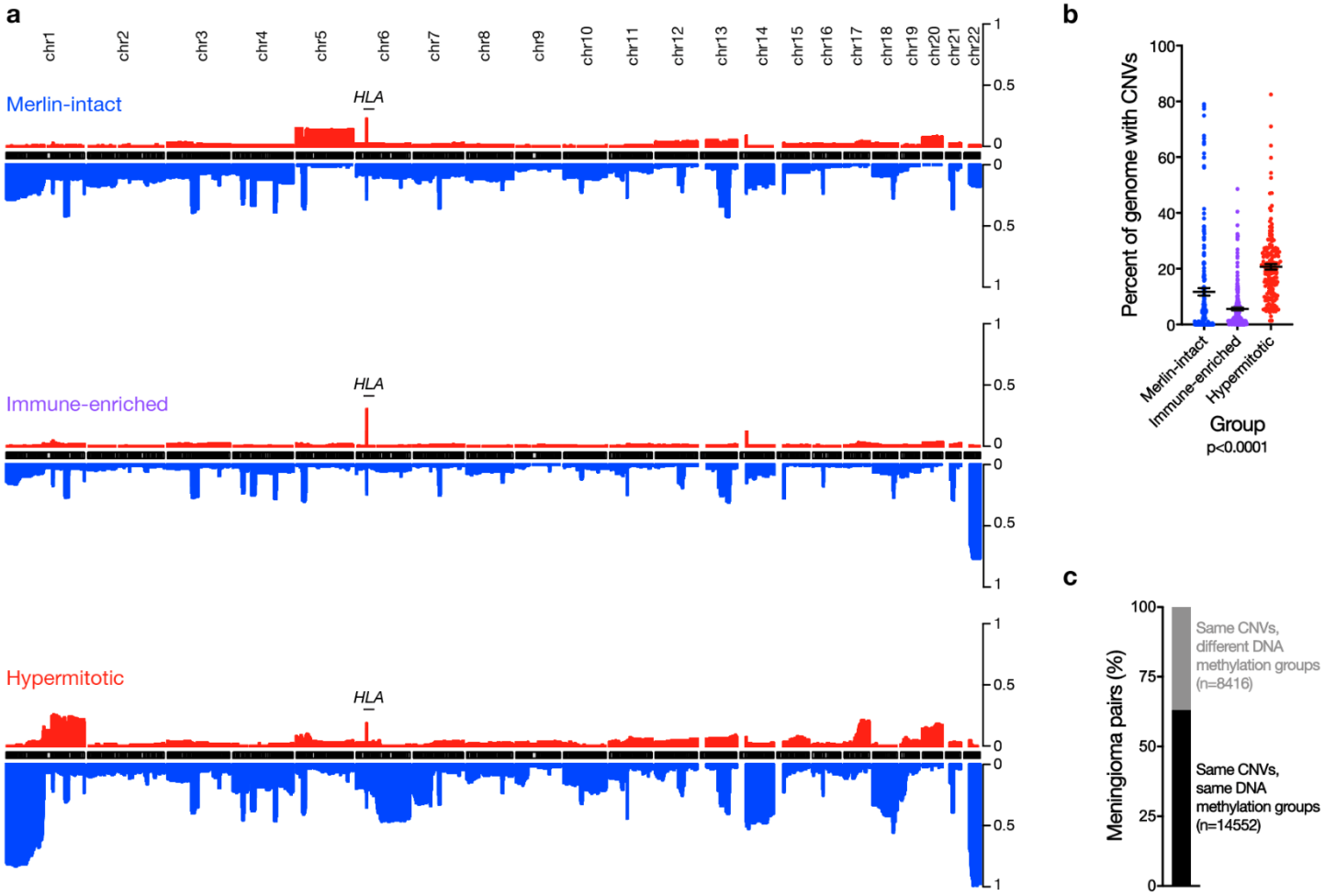

Supplementary figure 4. Genomic and cellular characteristics of Immune-enriched meningiomas.
a, Meningioma RNA sequencing xCell immune score (n=200) across DNA methylation groups (ANOVA, one-sided). **b**, Meningioma RNA sequencing xCell scores (n=200) across DNA methylation groups for microenvironment and stroma (left), and individual immune cell types (right). **c**, Correlation of DNA methylation leukocyte fraction (SeSAMe) and RNA sequencing immune score (xCell) (n=200) across DNA methylation groups. **d,** Meningioma DNA methylation tumor purity (n=565) across DNA methylation groups (ANOVA, one-sided). **e**, Volcano plots of meningioma differential gene expression (n=200) across SeSAMe DNA methylation groups iteratively comparing one group versus the others, with gene ontology transcription factor (TF) perturbation analysis of differentially enriched (red) or suppressed (blue) genes (Wald test, two-sided, Benjamin-Hochberg adjustment for multiple comparisons). **f**, Volcano plots of meningioma differential gene expression (n=200) across 4 minfi DNA methylation groups iteratively comparing one group versus the others, with gene ontology TF perturbation analysis (combined scores) of differentially enriched (red) or suppressed (blue) genes. Lines represent means, and error bars represent standard error of the means.

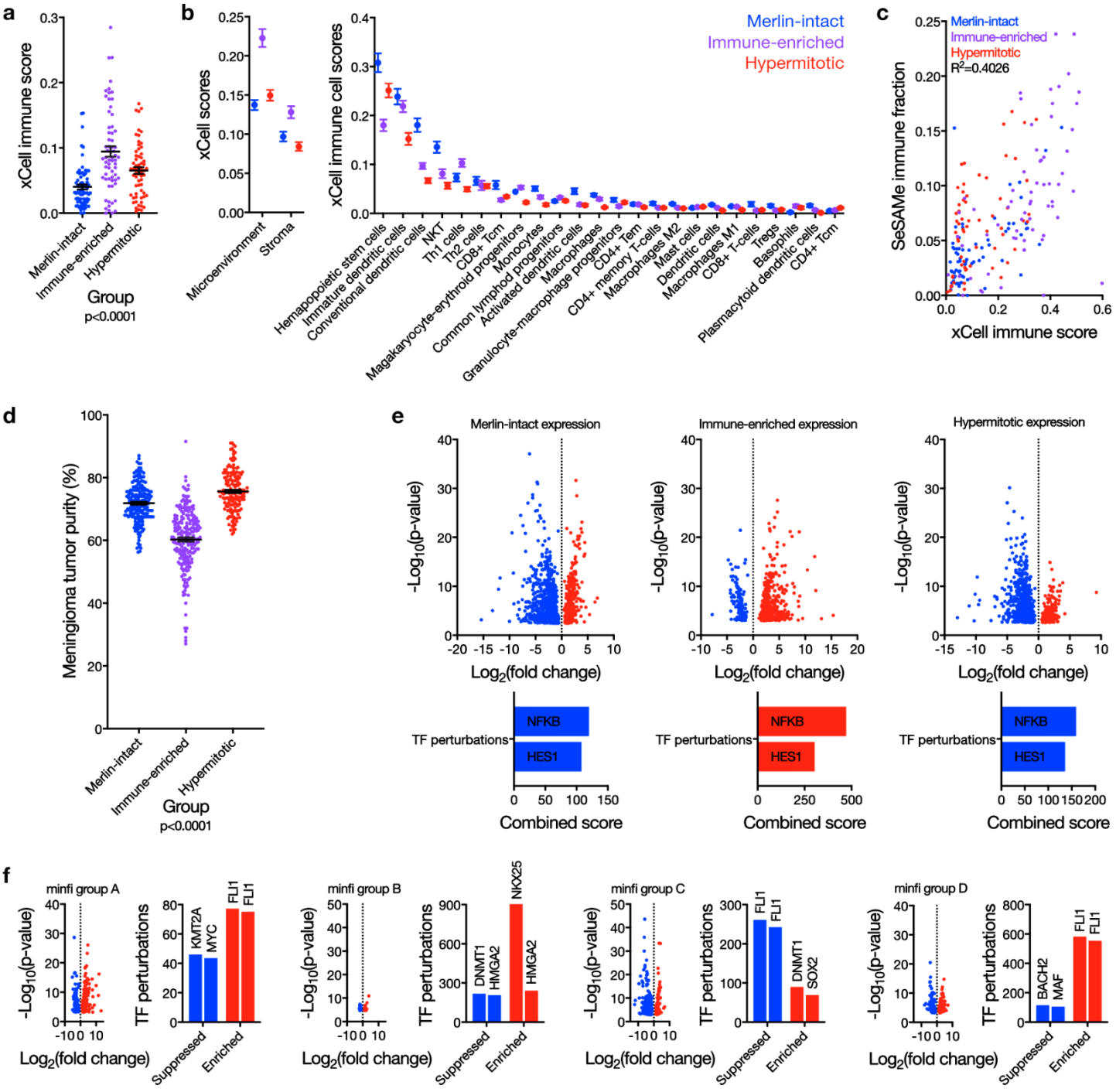

Supplementary figure 5. Meningioma single-cell RNA sequencing.
a, Cells in reduced dimensionality clusters from each sample analyzed using single-cell RNA sequencing. DNA methylation groups and chromosome 22q status of meningioma samples are annotated. **b**, UMAP of single-cell RNA sequencing transcriptomes of 57,114 cells from 8 human meningioma samples and 2 human dura samples, colored by sample of origin. **c**, UMAP of single-cell RNA sequencing transcriptomes from **b**, colored by cell cycle phase, as assigned by the 'CellCycleScoring' function in the Seurat R package.

a

Sample	DNA methylation group	22q status	C0	C1	C2	C3	C4	C5	C6	C7	C8	C9	C10	C11	C12	C13	C14	Total
MSC1	Merlin-intact	Intact	1441	191	11	152	17	46	28	6	5	578	19	29	11	3	1	2538
MSC2	Immune-enriched	Loss	8	0	2	710	0	34	5	8	0	86	22	11	0	21	7	914
MSC3	Hypermitotic	Loss	638	383	26	83	70	8	44	11	57	939	56	20	911	38	3	3287
MSC4	Merlin-intact	Intact	855	1353	13	774	10	188	2170	1787	23	354	88	70	62	58	65	7870
MSC4 dura	---	Intact	228	13	5	32	0	265	159	140	0	24	135	12	0	3	129	1145
MSC5	Immune-enriched	Loss	6680	1510	18	1198	39	83	181	363	11	38	65	7	181	18	30	10422
MSC5 brain/tumor interface	Immune-enriched	Loss	198	6315	28	748	5	64	282	260	80	85	56	180	226	27	14	8568
MSC5 dura	---	Intact	9	5	3	40	0	160	57	163	0	0	51	6	17	0	43	554
MSC6	Immune-enriched	Intact	28	7	2509	330	1783	2546	265	154	1109	60	905	90	0	173	415	10374
MSC6 brain/tumor interface	Immune-enriched	Intact	35	19	3364	1164	2662	230	278	252	1847	264	554	1507	0	691	304	13171
Total	---	---	10120	9796	5979	5231	4586	3624	3469	3144	3132	2428	1951	1932	1408	1032	1011	57114

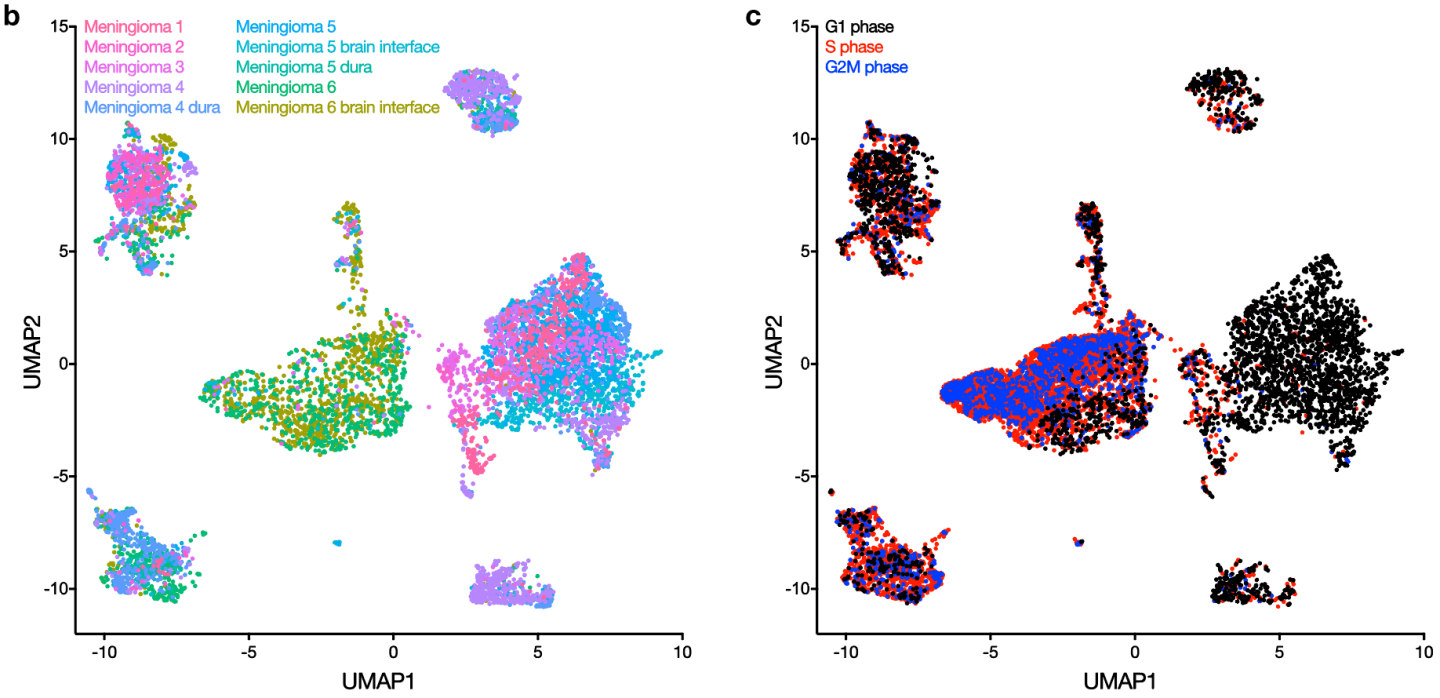

Supplementary figure 6. Meningioma single-cell transcriptome cell types.
a, Percentage of cells with loss of chromosome 22q (whole arm) in reduced dimensionality clusters identified using CONICSmat. Cells from meningioma samples with loss of chromosome 22q and from dura samples with intact chromosome 22q were used for this analysis. The pericyte cluster contained approximately equivalent proportions of cells with or without loss of chromosome 22q, suggesting this cluster may represent both normal and tumor cells in the perivascular space. **b**, Heatmap of differentially expressed genes across reduced dimensionality clusters, downsampled to 100 cells per cluster. **c**, Violin plots of marker gene expression across reduced dimensionality clusters. Lines represent means, and dotted lines represent quartiles.

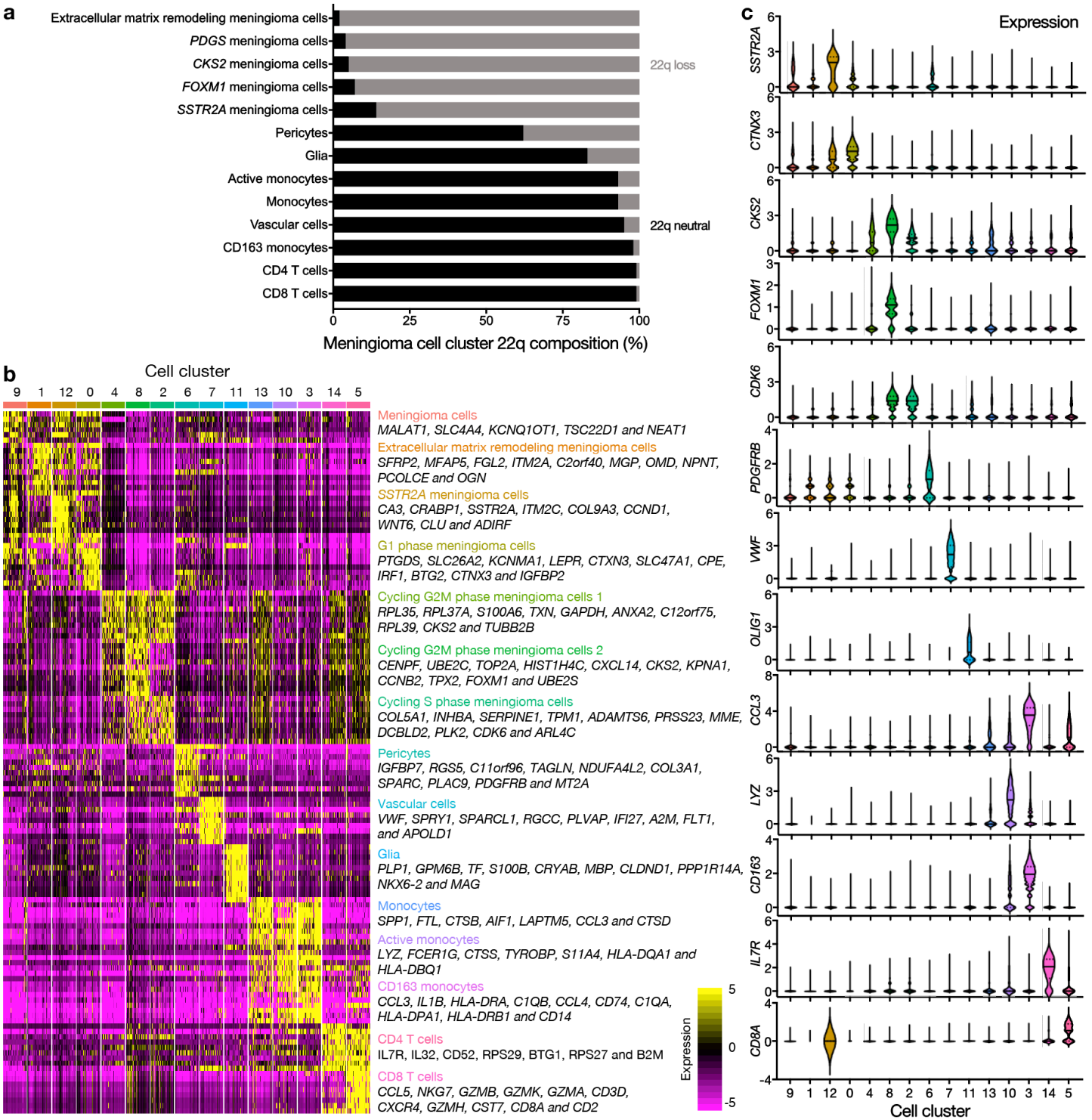

Supplementary figure 7. HLA expression underlies meningioma immune infiltration.
a, Meningioma DNA methylation tumor purity of 86 spatially-distinct samples from 13 meningiomas, nonoverlapping with the meningiomas from the discovery or validation cohorts, colored by DNA methylation group. **b**, Percentage of meningiomas with *HLA* loss of heterozygosity from whole-exome sequencing of non-Immune-enriched (n=11) and Immune-enriched (n=5) meningiomas (and paired normal samples) overlapping with the discovery cohort. **c**, Meningioma transcripts per million (TPM) expression of *HLA* genes encompassed by the polymorphic locus on chromosome 6p stratified by copy number status (entire locus of each gene amplified or deleted) across DNA methylation groups (n=200). Aggregating expression data by DNA methylation group (across all CNV contexts for each DNA methylation group) validated enrichment of *HLA-DRB5* ($p<0.0001$), *HLA-DRB1* ($p<0.0001$), *HLA-DQA1* ($p<0.0001$), and *HLA-DQB1* ($p<0.0001$) in Immune-enriched meningiomas compared to other groups (Student's t test, one-sided). **d**, Meningioma DNA methylation (n=565) of *HLA-DMA* (cg03531211) or *HLA-DPB1* (cg02286081) across DNA methylation groups (ANOVA, one-sided). **e**, Meningioma TPM expression (n=200) of *HLA-DMA* or *HLA-DPB1* across DNA methylation groups (ANOVA, one-sided). **f**, Correlated quantification of meningioma *HLA-DMA* ($R^2=0.44$, cg03531211) or *HLA-DPB1* ($R^2=0.12$, cg02286081) DNA methylation and TPM expression (n=200) across Merlin-intact (blue), Immune-enriched (purple), and Hypermitotic (red) DNA methylation groups. Lines represent means, and error bars represent standard error of the means. *$p\leq0.05$, **$p\leq0.01$, ***$p\leq0.0001$.

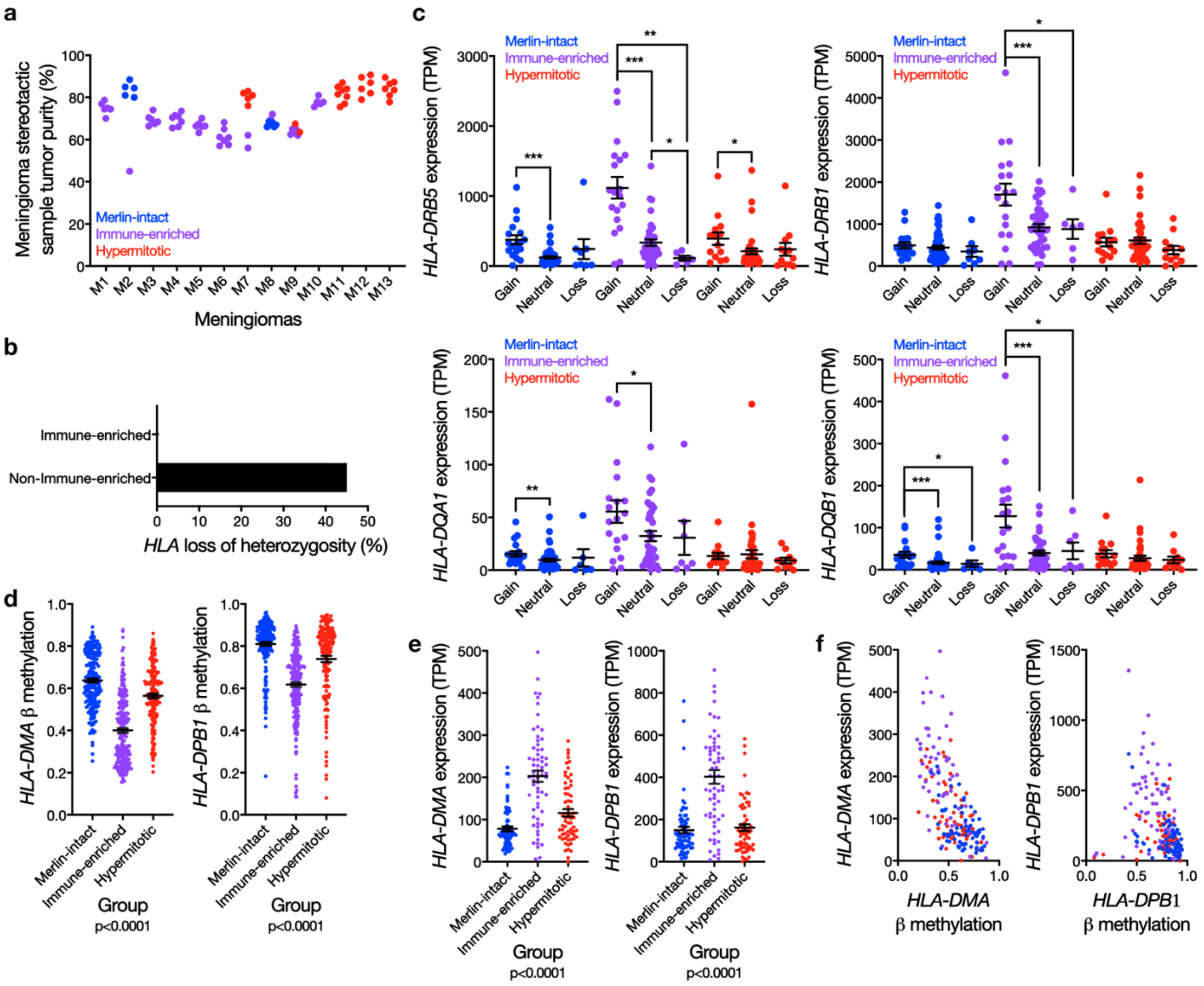

Supplementary figure 8. Hypermitotic meningiomas are distinguished by FOXM1 and FOXM1 target gene expression.

a, Gene ontology analysis of differentially expressed genes in Hypermitotic meningiomas compared to tumors from other DNA methylation groups. ChEA, ChIP-X Enrichment Analysis. **b**, Correlated quantification of meningioma Ki-67 and FOXM1 immunohistochemistry (n=92) across meningioma DNA methylation groups. **c**, Representative image of meningioma Ki-67 and FOXM1 confocal immunofluorescence microscopy. DNA is marked with DAPI. Scale bar 10 μM. **d**, Differential expression and gene ontology (ChEA 2016) analyses of Hypermitotic meningiomas with elevated Ki-67 labeling indexes (n=8, left/red), or of non-Hypermitotic meningiomas with elevated Ki-67 labeling indexes (n=9, right/grey), compared to non-Hypermitotic meningiomas with low Ki-67 labeling indexes (n=53). **e**, Heatmap of relative expression of FOXM1 target genes, nonoverlapping with E2F1 target genes, across meningioma DNA methylation groups (n=200). FOXM1 and E2F1 transcription factor targets were identified from the ChIP-X Enrichment Analysis (CHEA) dataset within the Harmonizome. SeSAMe meningioma DNA methylation groups are shown beneath the vertical dendrogram.

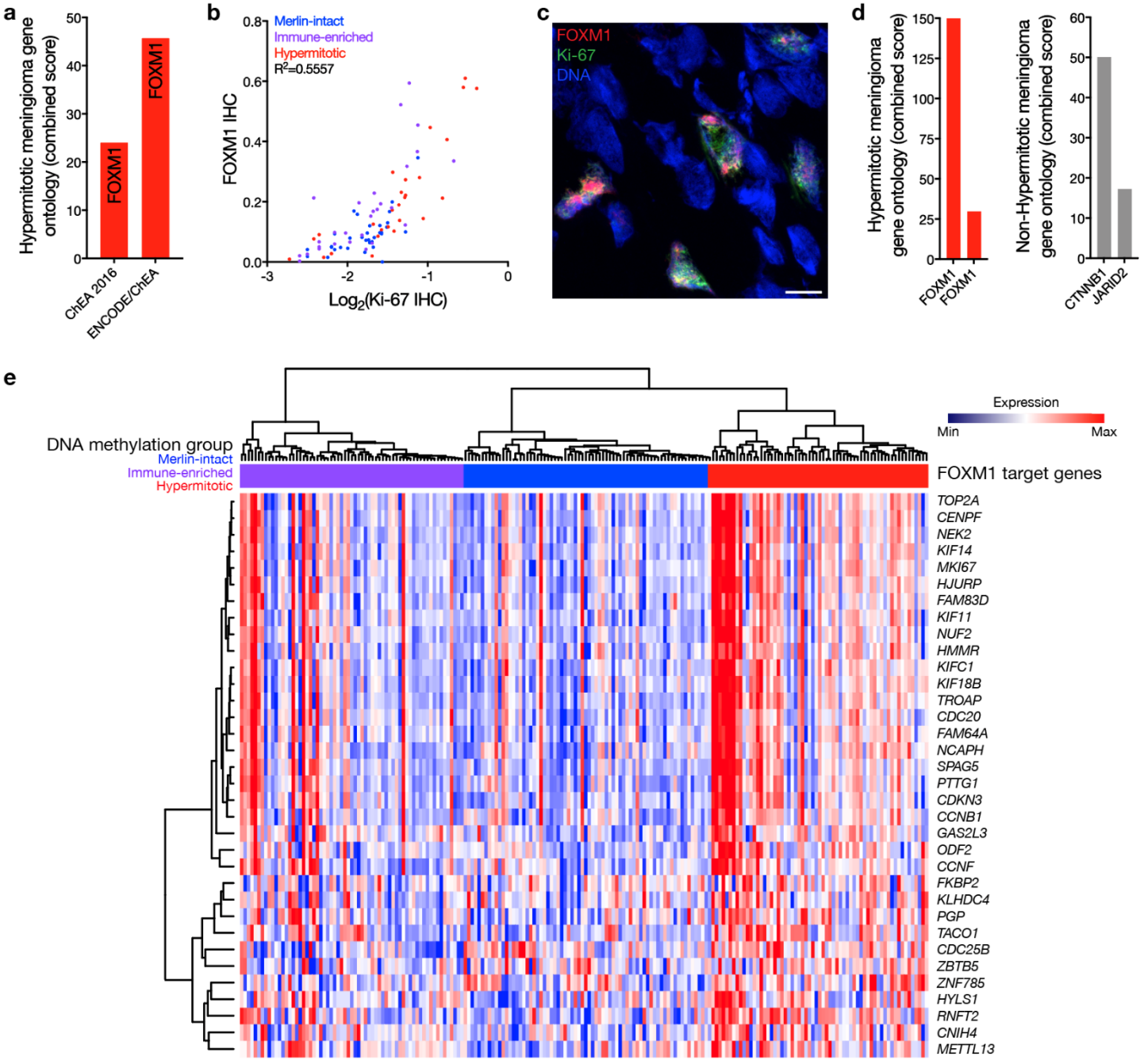

Supplementary figure 9. Meningioma DNA methylation groups are not distinguished by E2F1 target gene expression.

Heatmap of relative expression of E2F1 target genes, nonoverlapping with FOXM1 target genes, across meningioma DNA methylation groups (n=200). FOXM1 and E2F1 transcription factor targets were identified from the ChIP-X Enrichment Analysis (CHEA) dataset within the Harmonizome. SeSAMe meningioma DNA methylation groups are shown beneath the vertical dendrogram.

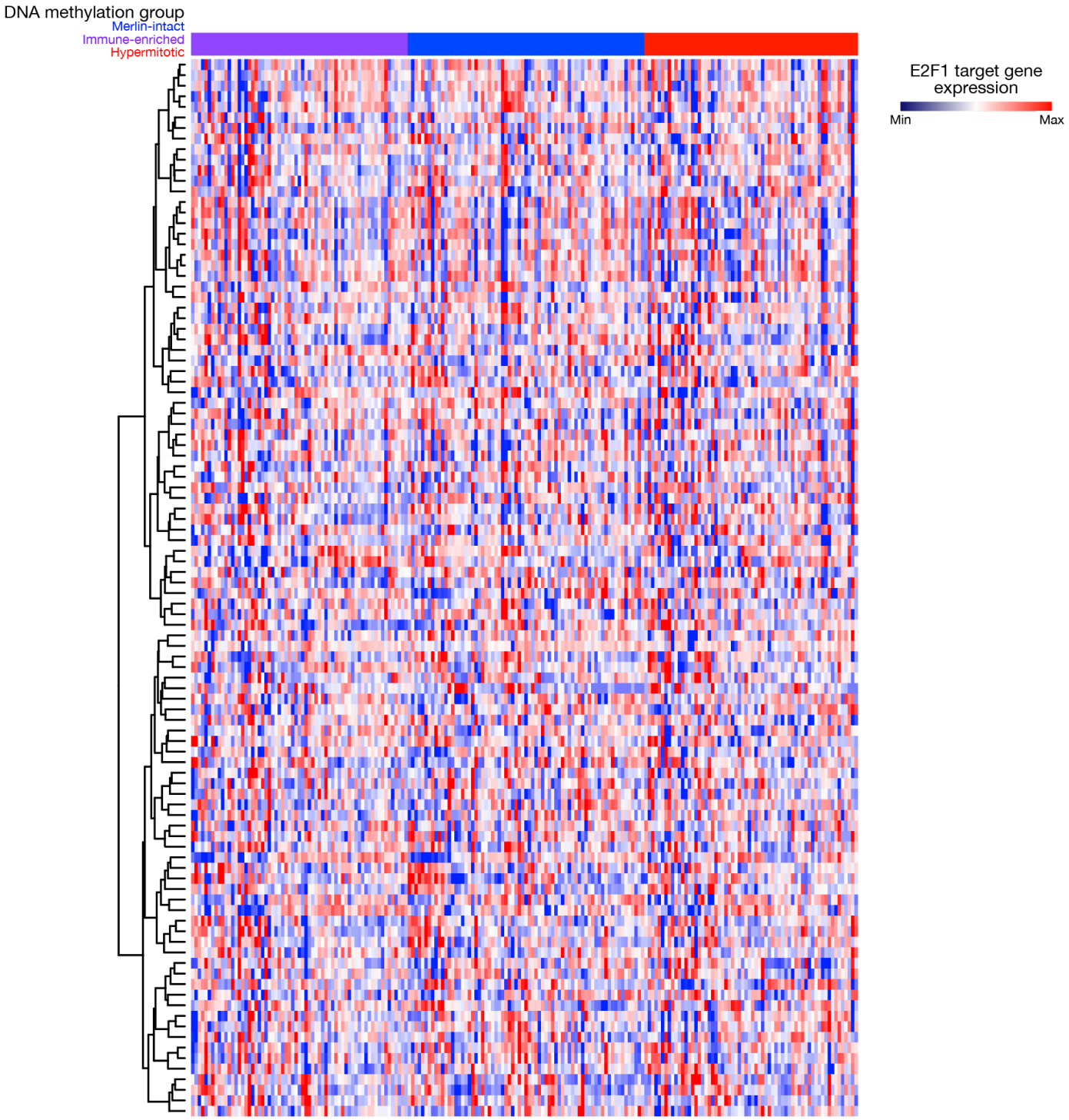

Supplementary figure 10. The enhancer landscape across meningioma DNA methylation groups.
a, Volcano plots of relative meningioma enhancer availability (n=25) across DNA methylation groups (top) from H3K27ac ChIP sequencing, and gene ontology analyses (bottom), of differentially enriched (red) or suppressed (blue) enhancers (Wald test, two-sided, Benjamin-Hochberg adjustment for multiple comparisons). ChEA, ChIP-X Enrichment Analysis. **b**, Volcano plots of meningioma relative super-enhancer availability (n=25) across DNA methylation groups (top), and gene ontology analyses (bottom), of differentially enriched (red) or suppressed (blue) super-enhancers (Wald test, two-sided, Benjamin-Hochberg adjustment for multiple comparisons). **c**, Meningioma transcripts per million (TPM) expression (n=200) of representative genes driving enhancer and super-enhancer ontologies from **a** and **b** across DNA methylation groups. Lines represent means, and error bars represent standard error of the means (ANOVA, one-sided).

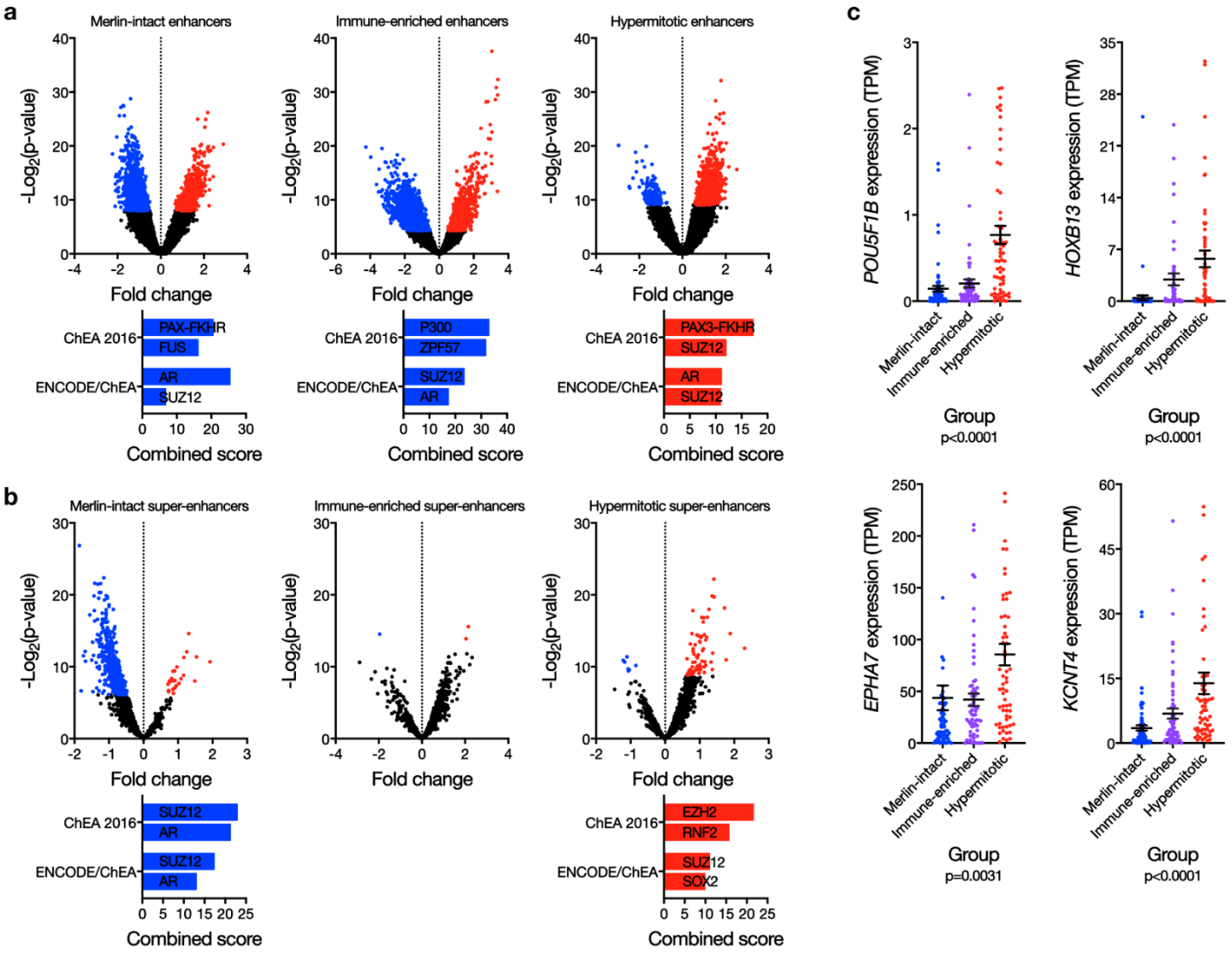

Supplementary figure 11. Loss of CDKN2A/B drives meningioma recurrence and meningioma cell proliferation.

a, Kaplan-Meier curve for meningioma local freedom from recurrence across DNA methylation groups stratified by *CDKN2A/B* copy number status derived from meningioma DNA methylation analysis of chromosome segment copy number deletions containing the entire *CDKN2A/B* locus (Log-rank test). The scarcity of *CDKN2A/B* losses in Merlin-intact or Immune-enriched meningiomas precluded robust survival analysis in these DNA methylation groups. Percentages refer to the proportion of meningiomas in each DNA methylation group with neutral or deleted chromosome segments containing the entire *CDKN2A/B* locus. **b**, QPCR for *CDKN2A* or *CDKN2B* in M10G$^{dCas9\text{-}KRAB}$ cells expressing a non-targeting control single-guide RNA (sgNTC), a single-guide RNA suppressing the p16^{INK4A} isoform of *CDKN2A* (sg*CDKN2A*), or a single-guide RNA suppressing *CDKN2B* (sg*CDKN2B*). 3 biological replicates per condition. **p=0.0002, ***p≤0.0001. (Student's t test, one-sided). **c**, Relative colony area of M10G$^{dCas9\text{-}KRAB}$ cells expressing sgNTC, sg*CDKN2A*, or sg*CDKN2B* after 10 days of clonogenic growth. 3 biological replicates per condition. *p=0.04, **p=0.02 (Student's t test, one-sided). Lines represent means, and error bars represent standard error of the means.

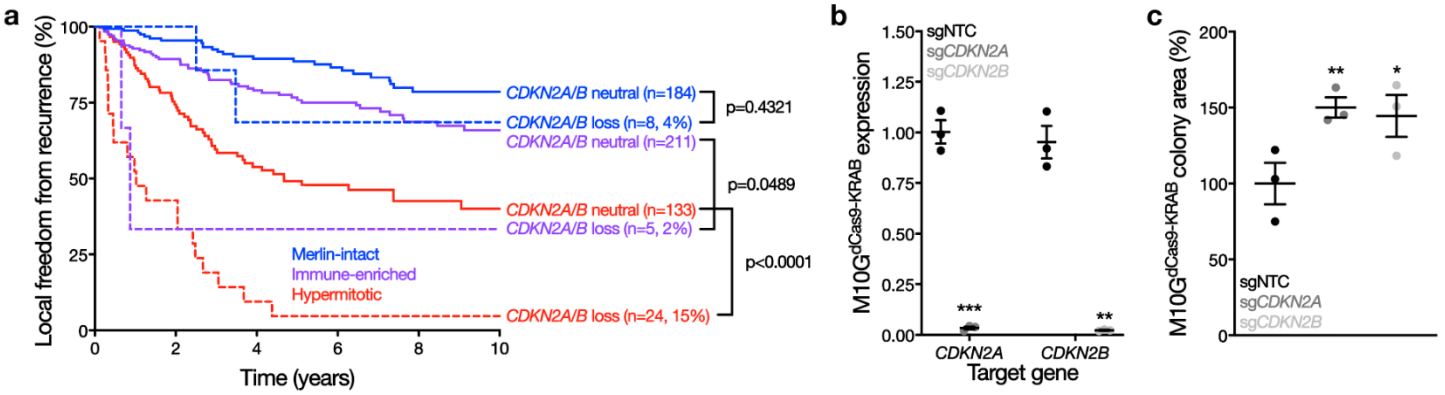

Supplementary figure 12. The transcriptomic landscape across meningioma DNA methylation groups. Unsupervised hierarchical clustering of meningiomas (n=200) using 2,000 differentially expressed genes. SeSAMe meningioma DNA methylation groups are shown between the RNA sequencing vertical dendrogram and relative RNA sequencing gene expression in the heatmap.

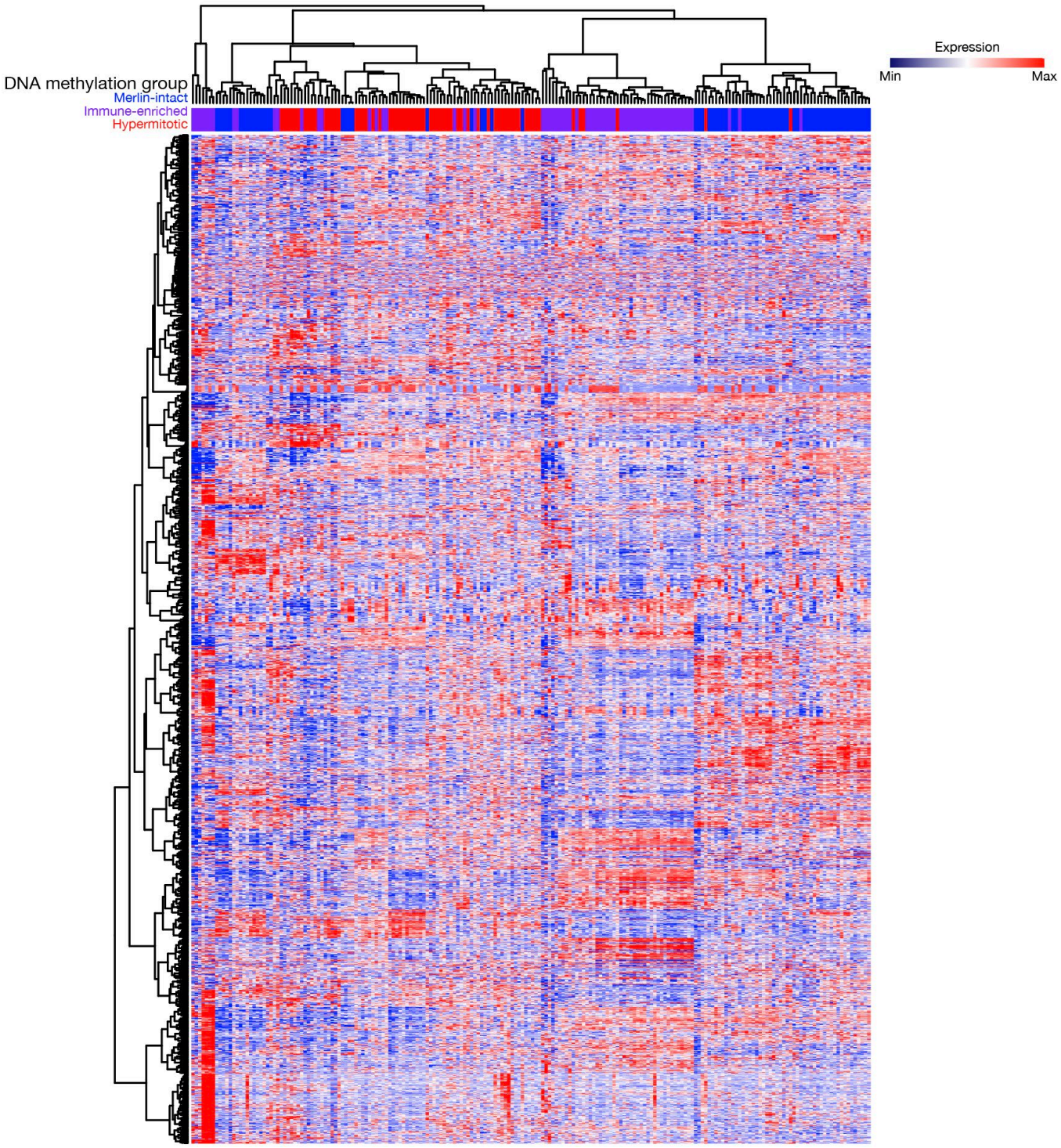

Supplementary figure 13. USF1 binds and activates the CDK6 promoter to drive meningioma recurrence and meningioma cell proliferation.

a, H3K27ac ChIP sequencing tracks of the *CDK6* locus in meningiomas (n=25) compared to normal neural cell and tissue samples (ChIP Atlas). **b**, Kaplan-Meier curve for meningioma local freedom from recurrence across DNA methylation groups stratified by chromosome 1q segment amplifications containing the entire *USF1* locus (Log-rank test). The absence of chromosome 1q segment amplifications in Merlin-intact meningiomas, and the scarcity of chromosome 1q segment amplifications in Immune-enriched meningiomas, precluded robust survival analysis in these DNA methylation groups. Percentages refer to the proportion of meningiomas in each DNA methylation group with neutral or amplified chromosome 1q segments containing the entire *USF1* locus. **c**, ChIP-QPCR after USF1 pulldown in DI134 meningioma cells for the *CDK6* promoter compared to negative control primers targeting a gene desert (NC1) or a gene not predicted to be bound by USF1 (NC2) from ChIP sequencing (Supplementary Table 11). From left to right, 2, 3, 3, 2, 3, or 3 biological replicates are shown. **p=0.002 (Student's t test, one-sided). **d**, QPCR for *USF1* in M10G$^{dCas9\text{-}KRAB}$ cells expressing sgNTC or a single-guide RNA suppressing *USF1* (sg*USF1*), or M10G cells over-expressing *USF1* or empty vector (EV). 3 biological replicates per condition. **p=0.0002, ***p≤0.0001 (Student's t tests, one-sided). **e**, QPCR for *USF1* in CH-157MN cells stably over-expressing USF1 or EV. 3 biological replicates per condition. ***p≤0.0001 (Student's t test, one-sided). Lines represent means, and error bars represent standard error of the means.

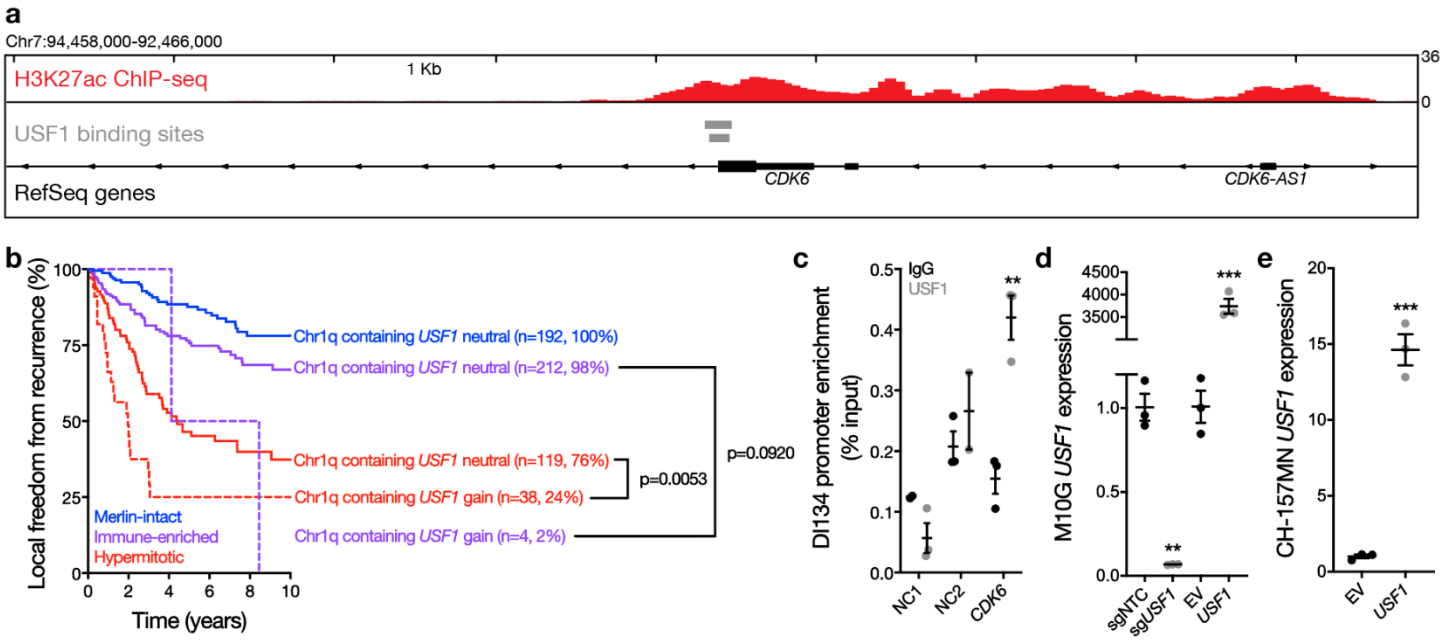

Supplementary figure 14. Cell cycle inhibition blocks meningioma growth in patients.
a, b, Magnetic resonance imaging and molecular features of meningiomas (left) that were resistant to cytotoxic therapies but responded to cytostatic cell cycle inhibition (right).

a

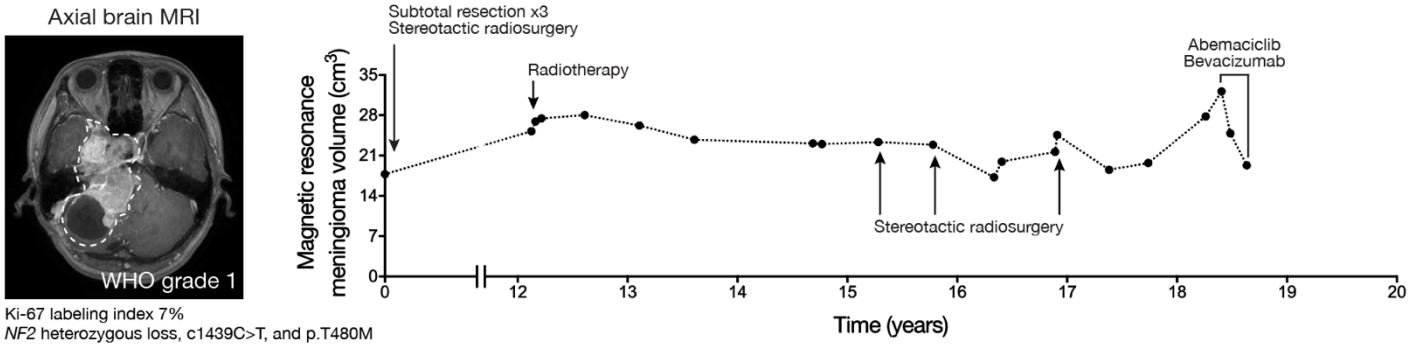

Ki-67 labeling index 7%
NF2 heterozygous loss, c1439C>T, and p.T480M
1p, 2q, 12q, 18p and 22q loss
Hypermitotic

b

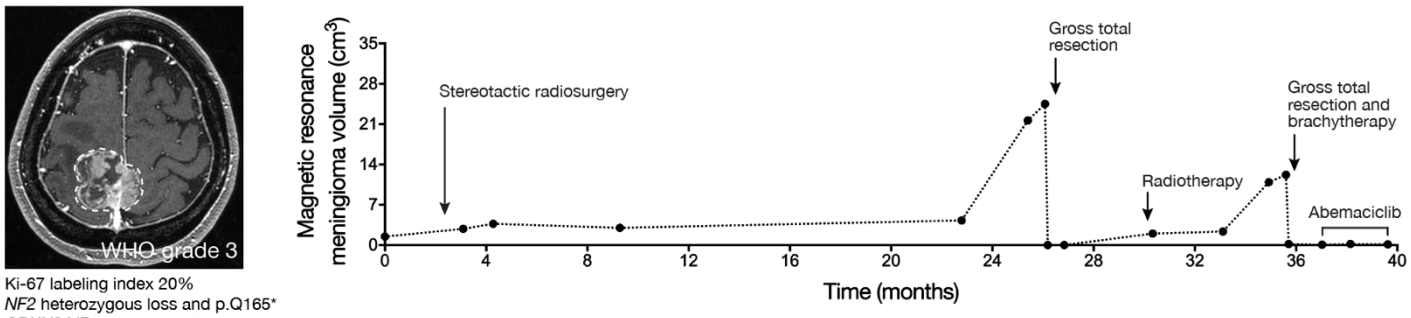

Ki-67 labeling index 20%
NF2 heterozygous loss and p.Q165*
CDKN2A/B homozygous loss
1p, 2, 3q, 4, 6q, 7, 8p, 9p, 10, 11, 14q, 15q, 18, 20q and 22q loss
Hypermitotic

Supplementary figure 15. Prognostic models based on meningioma CNVs.
a, Comparison of observed and predicted 5-year local freedom from recurrence (LFFR, n=201) from a model incorporating clinical features and DNA methylation groups (Figure 5d). Blue asterisks on the calibration curve denote the bootstrap optimism-corrected estimated probabilities. Lines represent means, and error bars represent standard error of the means. **b**, Recursive partitioning analysis of meningiomas (n=565) by CNVs reveals 3 CNV groups. **c**, Comparison of observed and predicted 5-year LFFR from a model incorporating clinical features and CNV groups (left, n=201), used to generate a nomogram for meningioma LFFR (right, https://william-c-chen.shinyapps.io/RaleighLab_CNVSubgroupNomogram/). Variables contribute points (top row), which estimate the probably of 5-year LFFR (bottom rows). **d**, Meningioma DNA methylation groups and WHO grades (n=565) across CNV groups (Chi-squared tests, two-sided). **e**, Kaplan-Meier curves for meningioma local freedom from recurrence and overall survival (n=565) comparing DNA methylation and CNV groups. Lines represent means, and error bars represent standard error of the means.

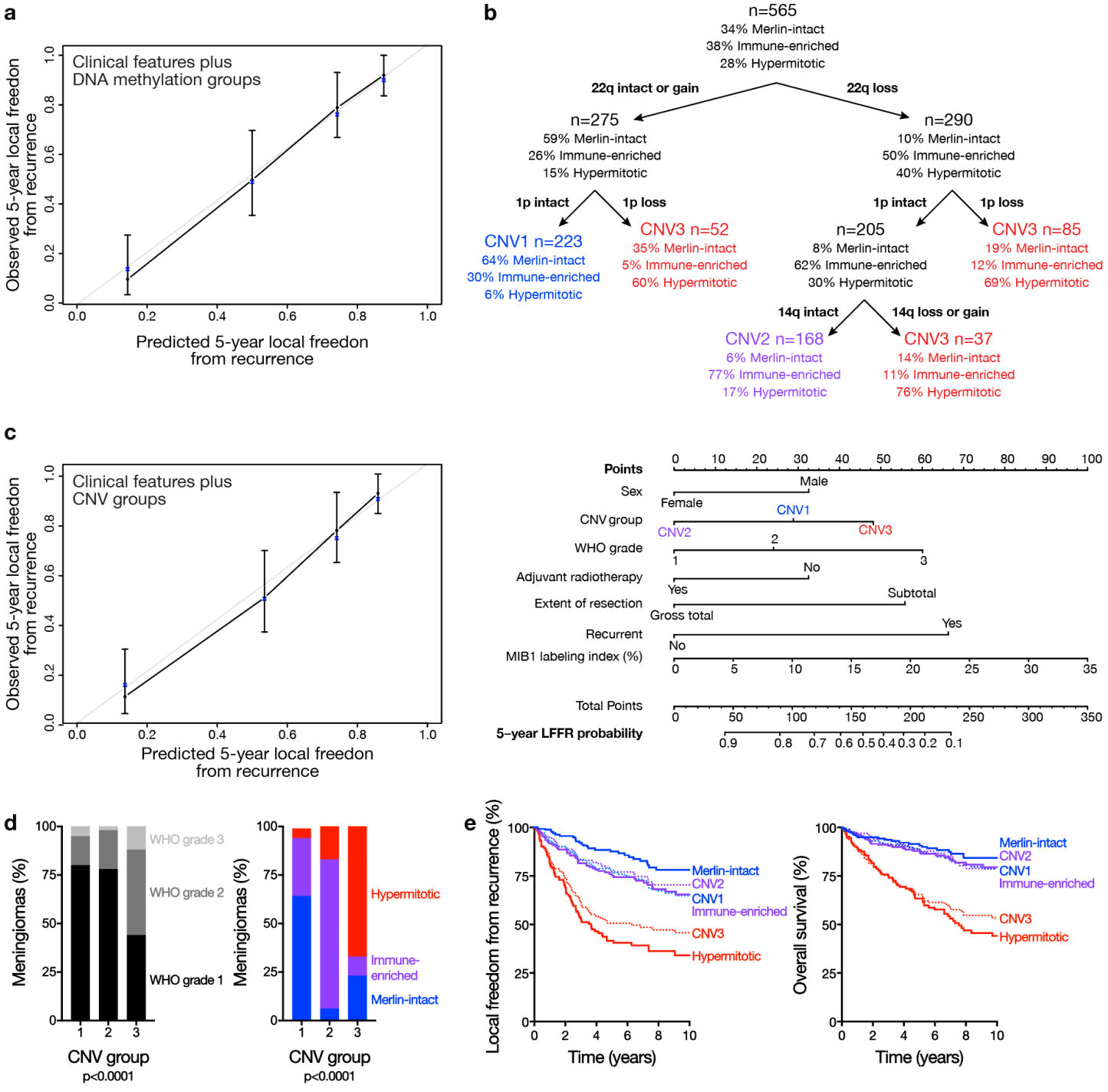

Supplementary figure 16. Prognostic models based on meningioma clinical features.
Comparison of observed and predicted 5-year LFFR from a model incorporating clinical features (left, n=201), used to generate a nomogram for meningioma LFFR (right, https://william-c-chen.shinyapps.io/RaleighLab_ClinicalVariablesNomogram/). Lines represent means, and error bars represent standard error of the means.

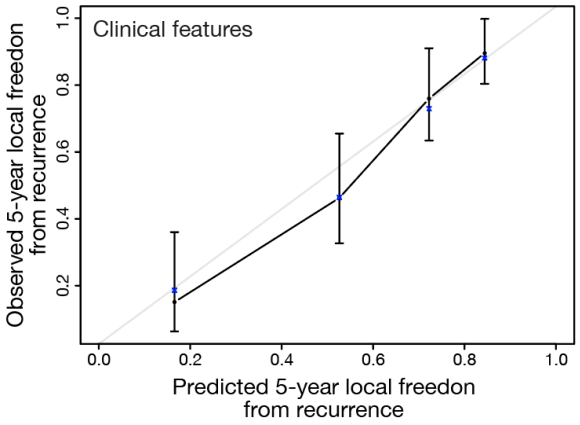

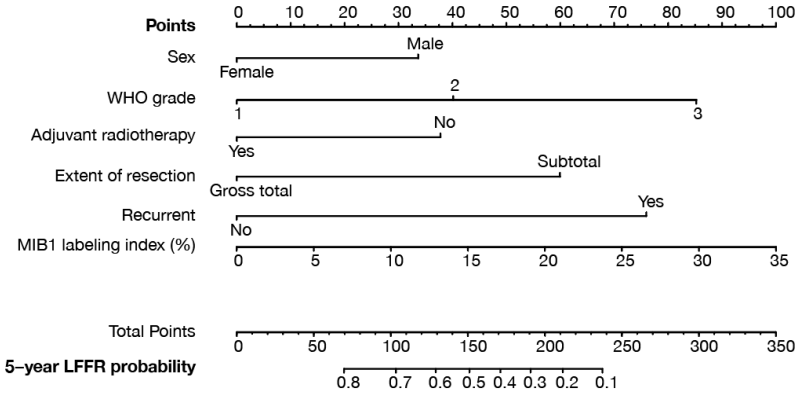

Supplementary note

Methods

Meningioma nucleic acid extraction

Frozen meningiomas were mechanically lysed using a TissueLyser II (QIAGEN) according to the manufacturer's instructions. DNA and RNA were extracted from lysed tissue using the AllPrep DNA/RNA/miRNA Universal Kit (#80224, QIAGEN). DNA and RNA quality were initially assessed using a NanoDrop One (Thermo Fisher Scientific). DNA samples with 260/280 values less than 1.8 or 260/230 values less than 1.6 were cleaned using ethanol precipitation and re-assessed. RNA samples with 260/280 values less than 1.8 or 260/230 values less than 1.6 were cleaned using the RNA Cleanup protocol from the RNeasy Mini Kit (#74106, QIAGEN). RNA samples were analyzed on a Bioanalyzer 2100 using the RNA 6000 Nano Kit (#5067-1511, Agilent Technologies). Only meningioma samples with high-quality DNA (260/280 greater than 1.8 and 260/230 greater than 1.6) and high-quality RNA (RIN greater than 8) were used for DNA methylation profiling and RNA sequencing. After quality control, the discovery cohort was comprised of 200 meningiomas from patients who were treated at UCSF from 1991 to 2016 (median clinical follow-up 6.3 years), and the validation cohort was comprised of 365 consecutive meningiomas from patients who were treated at HKU from 2000 to 2019 (median clinical follow-up 5.3 years).

DNA methylation profiling and analysis

Sampling distributions of DNA methylation group proportions were generated via bootstrapping. In brief, the population size of the discovery cohort was sampled with replacement 100 times, and the proportion of meningiomas in each DNA methylation group was calculated for each sampling iteration. K-means consensus clustering was performed to determine the optimal number of clusters using the ConsensusClusterPlus R package (Bioconductor v3.10)[1], subsampling 1000 times per cluster number using all 2,000 probes and 80% of samples per subsample, and validated using continuous distribution functions. To quantify differences in SeSAMe and mini preprocessing pipelines, a signal-to-noise ratio (SNR) was calculated using *NF2* copy number status across meningioma DNA methylation groups, where signal = (*NF2* intact in Merlin-intact meningiomas) + (*NF2* loss in non-Merlin-intact meningiomas) and noise = (*NF2* loss in Merlin-intact meningiomas) + (*NF2* intact in non-Merlin-intact meningiomas). A SNR was calculated 3 times across 3 minfi meningioma DNA methylation groups, assuming each group was Merlin-intact in turn, and the most favorable minifi SNR was reported, which remained worse than the SNR for 3 SeSAMe meningioma DNA methylation groups. The same approach was used for 4 minfi meningioma DNA methylation groups. In sum, the SNR for *NF2* copy number status was 2.25 for 3 minfi groups, 5.35 for 4 minfi groups, and 5.57 for 3 SeSAMe groups.

DNA methylation profiles from representative meningiomas and meningioma cell lines were compared in reduced dimensionality space using the Rtsne R package (v0.15). A matrix of the samples and their β methylation values for the 2,000 variable probes were used as input and the 'Rtsne' command was run with the parameters 'pca=F, normalize=F, perplexity=3.'

Leukocyte percentage within the tumor samples was calculated from DNA methylation using the 'estimateLeukocyte' command within the SeSAMe R package[2]. In brief, the intensity of DNA methylation probes uniquely hyper- or hypo-methylated in leukocytes were used to estimate the leukocyte percentage. Tumor purity was estimated from DNA methylation profiles using the PAMES R package (v2.6.2)[3]. To generate cross-platform comparable DNA methylation profiles on meningiomas and normal tissue samples from meningioma patients (muscle or fat), β methylation values of adjacent CpG sites were combined and the sites were reduced to genomic regions, with a minimum of 3 CpG sites per region. Methylation status of genomic regions was used to compute the Area Under the Curve (AUC) to define the segregation between tumor and normal samples. Hypermethylated and hypomethylated genomic regions with the top 10 AUCs (20 regions in total) were selected for tumor purity estimation. These regions were completely methylated or unmethylated in normal tissue samples, but were partially methylated in meningiomas. The median of partial methylation across these regions in meningiomas was used to estimate tumor purity.

Copy number variant analysis

To validate CNVs derived from DNA methylation profiles, chromosomal losses and gains from DNA methylation profiles were compared to those from whole-exome sequencing of 25 previously described meningiomas overlapping with the discovery cohort[4], and to CNVs from *de novo* Clinical Laboratory Improvement Amendments (CLIA)-certified exome sequencing of 10 spatially distinct meningioma samples[5,6] (3 Merlin-intact, 15 Immune-enriched, and 17 Hypermitotic meningiomas). To define CNVs from previously described

meningioma whole exome sequences and from *de novo* CLIA-certified exome sequences, reads were aligned with the Burrows-Wheeler Aligner (BWA)[7], deduplicated using the Genome Analysis Toolkit (GATK)[8,9], and large-scale copy number alterations were called using CNVkit[10]. CNVs were 99.12% concordant across research and clinical bioinformatic platforms using DNA methylation and exome sequences approaches.

The interdependence of CNVs and meningioma DNA methylation groups was analyzed by identifying pairs of meningiomas with identical CNV profiles, and subsequently comparing the DNA methylation profile between meningioma pairs. This approach revealed 37% of meningioma pairs with identical CNVs were assigned to different DNA methylation groups.

CNVs of biologic interest across meningioma DNA methylation groups (*NF2*, *HLA, CDKN2A/B,* or *USF1*) were focal (<5 Mb) or non-focal for *HLA* or *CDKN2A/B*, or predominantly non-focal for *NF2* (n=350 of 351 meningiomas) or *USF1* (n=40 of 42 meningiomas). Definitions of CNV focality lack consensus, specifically regarding how to define focal CNVs containing single genes of different sizes (*CDKN2A, CDKN2B, NF2, USF1*), and how to define focal CNVs containing polymorphic loci comprised of multiple genes of different sizes (*HLA-DRB5, HLA-DRB1, HLA-DQA1, HLA-DQB1*). For meningiomas, non-focal CNVs deleting chromosome 22q segments containing *NF2* are widely recognized as having biologic significance due (at least in part) to deletion of *NF2* despite the fact that these deletions are often broad. Thus, we decided it would be appropriate to combine and quantify focal plus non-focal CNVs containing other loci of biologic interest across meningioma DNA methylation groups, provided we could orthogonally corroborate the biologic significance of genes of interest encompassed by these loci. Considering the resolution of CNVs derived from Illumina 850k DNA methylation arrays (which are based on probe locations, rather than sequencing reads), we decided the most parsimonious and transparent approach would be to quantify and report only CNVs containing entire loci of interest. Thus, whether focal or non-focal, CNVs were included for analysis across meningioma DNA methylation groups only when the entire gene or locus of interest was gained or lost, but to ensure our analyses were robust and legitimate, secondary analyses including CNVs partially overlapping with loci of interest were performed and are described below. The same approach was used to analyze of the polymorphic *HLA* locus on chromosome 6p, which encompassed the *HLA-DRB5, HLA-DRB1, HLA-DQA1,* and *HLA-DQB1* genes. The polymorphic *HLA* locus was defined as Chr6:32475000-32725000 (hg19) via manual inspection of the combined distribution of losses and gains containing the *HLA* locus, and identification of recurrent breakpoints surrounding the region of increased polymorphism.

As an additional test of CNV specificity across meningioma DNA methylation groups, focal deletions <5 Mb of the entire *CDKN2A/B* locus were more common in Hypermitotic meningiomas compared to other DNA methylation groups (5 *CDKN2A/B* deletions in 157 Hypermitotic meningiomas compared to 3 deletions in 408 non-Hypermitotic meningiomas, p=0.0413, Fisher's exact test). Focal amplifications <5 Mb of the entire polymorphic *HLA* locus were more common in Immune-enriched meningiomas compared to other DNA methylation groups (n=37 of 216 Immune-enriched meningiomas, n=20 of 192 Merlin-intact meningiomas, n=8 of 157 Hypermitotic meningiomas, p=0.0013, Chi-squared test). There were 5 meningiomas with partial deletions of the *CDKN2A/B* locus, which, when combined with CNVs deleting the entire *CDKN2A/B* locus, preserved the trends and statistical significance across DNA methylation groups presented in the main text (n=28 of 157 Hypermitotic meningiomas, n=8 of 192 Merlin-intact meningiomas, n=6 of 216 Immune-enriched meningiomas, p<0.0001, Chi-squared test). There were 55 meningiomas with partial amplifications of the polymorphic *HLA* locus, which, when combined with CNVs amplifying the entire polymorphic *HLA* locus, preserved the trends and statistical significance across DNA methylation groups presented in the main text (n=64 of 216 Immune-enriched meningiomas, n=33 of 192 Merlin-intact meningiomas, n=28 of 157 Hypermitotic meningiomas, p=0.0033, Chi-squared test). There were 8 meningiomas with partial deletions of the polymorphic *HLA* locus, which, when combined with CNVs deleting the entire polymorphic *HLA* locus, preserved the trends and statistical significance across DNA methylation groups presented in the main text (n=25 of 216 Immune-enriched meningiomas, n=28 of 192 Merlin-intact meningiomas, n=33 of 157 Hypermitotic meningiomas, p=0.0412, Chi-squared test).

RNA sequencing and analysis

Differential expression analysis was performed in R with DESeq2 (Bioconductor v3.10)[11], using the 'apeglm' parameter[12] to calculate log fold changes and setting a false discovery rate of 0.05. Differentially expressed genes were identified as those with log fold changes greater than 1 and an adjusted p-value less than 0.05. Gene ontology analysis of differentially expressed genes was performed using Enrichr, and combined scores displayed represent z-score weighted p-values, which lack error bars[13,14].

Cell types within samples were deconvoluted using xCell with transcripts per million values[15]. In brief, the strength of gene expression patterns unique to different cell types were used to estimate the proportion of cell types within each meningioma.

The variance stabilizing transformation of the RNA sequencing counts were used to calculate variances for each gene across the 200 meningioma samples. The 2,000 most variable genes were used for unsupervised hierarchical clustering (Pearson correlation distance, Ward's method), which did not reveal any clear clusters of genes or meningiomas. Moreover, transcriptome clustering failed to recapitulate DNA methylation groups.

The specificity of FOXM1 signaling in Hypermitotic meningiomas was assessed by differential expression and gene ontology analysis between (i) Hypermitotic meningiomas with Ki-67 labeling indexes greater than 13% (n=8) and non-Hypermitotic meningiomas with Ki-67 labeling indexes less than 5% (n=53), or between (ii) non-Hypermitotic meningiomas with Ki-67 labeling indexes greater than 13% (n=9) and non-Hypermitotic meningiomas with Ki-67 labeling indexes less than 5% (n=53). Ki-67 labeling index upper and lower thresholders were defined by the third quartile in Hypermitotic meningiomas (13%), and the average in non-Hypermitotic meningiomas (5%), respectively. FOXM1 and E2F1 transcription factor targets were identified from the ChIP-X Enrichment Analysis (CHEA) dataset within the Harmonizome[16], and compared across meningioma DNA methylation groups.

Somatic short variant sequencing and analysis

Genomic DNA was processed using this panel and the CleanPlex Target Enrichment and Library Preparation kit following manufacturer's instructions (#PGD364, Paragon Genomics) for *NF2* sequencing. Library quality was assessed on a TapeStation 4200 using the High Sensitivity D1000 Kit (#5067-5584, Agilent Technologies). 150 bp paired-end reads were sequenced on an Illumina MiSeq v2 Micro at the UCSF Center for Advanced Technology. Quality control of FASTQ files was performed with FASTQC[17]. Reads were mapped to the *NF2* locus using Bowtie2[18]. Somatic short variants (point mutations and small indels) were identified using the Genome Analysis Toolkit (GATK)[19]. The mapped Bowtie2 output was processed with recalibration of base confidence scores, and processed reads were used as input for HaplotypeCaller[8] with the parameters '-ERC none' and '--max-reads-per-alignment-start 0' to identify somatic variants. Somatic short variants were filtered for a minimum total depth of 100 reads. Filtered variants were annotated using SnpEff[20,21], and all but one *NF2* somatic short variant identified across DNA methylation groups were predicted to have 'HIGH' variant impact.

Somatic short variants in *TRAF7* were identified from the RNA sequencing data by following the Genome Analysis Toolkit's (GATK)[19] "RNAseq short variant discovery" Best Practices Workflow. In brief, the mapped HISAT output was processed by de-duplication and recalibration of base confidence scores. Processed reads were used as input for HaplotypeCaller[8] with the parameters '--dont-use-soft-clipped-bases true' and '-stand-call-conf 20' to identify somatic short variants. The 'VariantFiltration' command within GATK was used to further filter the identified variants with the parameters '-window 35 -cluster 3 --filter-name "FS" -filter "FS > 30.0" --filter-name "QD" -filter "QD < 2.0".' Filtered variants were annotated using SnpEff[20,21]. The same pipeline was attempted to identify somatic short variants in *PIK3CA*, *SMARCB1*, *SMO*, *KLF4*, *POLR2A*, *NF2*, and *AKT1*. Low coverage (average FPKM<10 across samples) excluded *PIK3CA*, *AKT1*, and *NF2* from further analysis. The small number of mutations (<10) detected in *SMARCB1*, *KLF4*, and *POLR2A* could not be distinguished from background error rates in RNA sequencing. Finally, mutations identified in *SMO* were unlikely to be activating mutations[22], and were discordant from prior studies[23], likely to be spurious findings. Thus, only somatic short variants in *TRAF7* were reported.

To generalize our analysis of meningioma short somatic variants across DNA methylation groups, 53 meningiomas with matched exome sequencing and DNA methylation profiling were analyzed for recurrent variants enriched in meningiomas[24–26]. Samples included 43 previously described meningioma whole exomes[4,27], 25 of which overlapped with the discovery cohort, and 10 spatially distinct meningioma samples analyzed *de novo* using CLIA-certified exome sequencing of 500 genes, including all recurrently mutated genes reported in meningiomas, such as *TRAF7*, *AKT1*, *SMO*, *KLF4*, *CDKN2A/B*, *TERT, SMARCB1, BAP1, SUFU, TP53, PTEN, MYC, PBRM1, and PIK3CA*[5,6] (6 Merlin-intact, 21 Immune-enriched, and 26 Hypermitotic meningiomas). Short somatic variants were defined as previously described[4,5,27]. In brief, whole exome sequences were aligned with the Burrows-Wheeler Aligner (BWA)[7] and analyzed using Picard tools and the Genome Analysis Toolkit (GATK), following GATK Best Practices[19].

Polysolver[28] and SOAP-HLA[29] were used to infer MHC class I genotypes (HLA-A, HLA-B, and HLA-C) from filtered whole exome sequencing data on 15 meningiomas with matched normal tissue whole exome sequencing data and DNA methylation profiling (5 Immune-enriched, 10 Hypermitotic). Mutant neoepitope peptide candidates between 8 to 11 amino acids in length were derived from missense mutations using ANNOVAR[30].

The half maximal inhibitory concentration (IC50) for binding between each mutant peptide and the 6 patient-specific, inferred MHC class I alleles were predicted using netMHCpan-4.010[31], and mutant peptide sequences deemed to be neoantigens met a standard cutoff of less than 500 nM for predicted IC50[32].

For HLA loss of heterozygosity analysis, whole exome capture and read sequencing were performed as previously described on 25 meningiomas overlapping with the discovery cohort (9 Immune-enriched, 16 non-Immune-enriched) with matched normal tissue controls[4]. Paired-end sequence data were aligned using the Burrows-Wheeler Aligner to the reference human genome build hg19[7]. Duplicate removal, base quality recalibration, and multiple-sequence realignment were performed using Picard suite and Genome Analysis Toolkit[8,9]. Exome HLA Class I genotyping was performed using Polysolver and SOAP-HLA[28,29].

Subcellular fractionation and immunoprecipitation

Subcellular fractionation kits were purchased from Thermo Fischer Scientific (#78833) and used according to manufacturer's instructions. In brief, M10G cells were seeded into 10cm plates, and trypsinised and lysed in Cytoplasmic Extraction Reagent I containing protease and phosphatase inhibitors after 2 days of growth. Lysis solution was incubated on ice for 10 minutes before addition of Cytoplasmic Extraction Reagent II and incubation for 1 minute. Cytoplasmic fractions were isolated via centrifugation for 5 minutes, 21,000x g, 4°C. The Nuclear pellet was resuspended in Nuclear Extraction Reagent containing protease and phosphatase inhibitors followed by incubation on ice for 40 minutes with intermittent vortexing. Finally, the nuclear fraction was isolated by centrifugation for 5 minutes, 21,000 x g, 4°C. Protein concentration was measured using Bradford Reagent (#5000205, Biorad), samples were normalized, and processed for immunoblotting or immunoprecipitation.

For whole cell lysate immunoprecipitation, samples were lysed in ice-cold Jies buffer (100mM $NaCl_2$, 20mM Tris HCl (pH7.5), 5mM $MgCl_2$, 0.5% NP40, protease and phosphatase inhibitors) before centrifugation at 4°C for 5 minutes, 21,000 x g. Protein concentration was measured using Bradford reagent and equal protein from each sample was loaded onto pre-washed FLAG M2 beads (#M8823, Sigma-Aldrich) before incubation at 4°C, overnight with gentle rotation. The following day, proteins were eluted from the beads with Laemmli buffer and boiled. Immunoblotting revealed IRF8 in cytoplasmic and nuclear fractions, and ARHGAP35 in cytoplasmic fractions.

Cell proliferation and apoptosis assays

Colorimetric proliferation assays were performed using the CellTiter 96 Non-Radioactive Cell Proliferation Assay (#G4100, Promega), according to manufacturer's instructions. For clonogenic assays, 150 cells were seeded in triplicate in 6 well plates. Cells were treated with either vehicle or drug both 1 and 6 days after seeding. After 10 total days of growth, cells were fixed in methanol for 30 minutes and stained with 0.01% crystal violet (C6158, Sigma-Aldrich) for 1 hour. Plates were rinsed with water three times, allowed to air dry, and imaged on a Zeiss Stemi 508 stereo microscope. Colony area was quantified by measuring total image intensity using ImageJ, with normalization to background intensity. Apoptosis assays were performed by treating cells with actinomycin D (#11421, Caymen Chemicals) 0.5 µg/ml for 24 hours.

Proteomic proximity-labeling mass spectrometry

To prepare cell pellets for biotin/streptavidin precipitation, samples were lysed in Urea buffer (8M urea, 0.1M Ammonium Bicarbonate pH8, 150mM NaCl, protease inhibitors and phosphatase inhibitors), sonicated for 1 minute followed by alkylation of free cysteines (10mM iodoacetamide). Trypsin digest (#V5073, Promega) was performed at 37°C for 20 hours with gentle rotation. Digested proteins were desalted through a 100mg Sep-Pak C18 vacuum cartridge (#WAT023590, Waters) and lyophilized in a speed vac. Lyophilised proteins were dissolved in IAP buffer (50 mM MOPS, 10 mM HNa2PO4, 50 mM NaCl, pH 7.5), sonicated for 30 minutes in a 4°C water bath and centrifuged to clear insoluble material. For biotin/streptavidin precipitation, 20 µl of washed anti-biotin beads (#ICP0615, Immunechem Pharmaceuticals) were incubated with each protein sample (2 hours, 4°C, gentle rotation), beads were washed and eluted in 0.15% trifluoroacetic acid, desalted on nest tips, and lyophilized prior to mass spectrometry.

Samples were resuspended in 4% formic acid, 4% acetonitrile solution, and separated by a reversed-phase gradient over a nanoflow column (360 µm O.D. x 75 µm I.D.) packed with 15 cm of 1.7 µm BEH C18 particles (#186002350, Waters). The HPLC buffers were 0.1% formic acid and 100% acetonitrile on 0.1% formic acid for buffer A and B respectively. The gradient was operated at 300 nL/min from 5 to 25% buffer B over 36 min, followed by a 25%-36%B over 42 min, a column wash at 95% B, with a total acquisition time of 90 min. Eluting peptides were analyzed in on a Orbitrap Fusion Lumos Tribrid Mass Spectrometer system (Thermo Fischer Scientific) equipped with a n1200 Easy-nLC 1200 high-pressure liquid chromatography system (Thermo Fischer

Scientific). A data-dependent acquisition method was used with following parameters: 1 second cycle time, MS1 acquisition in the orbitrap with 350-1350 m/z range at 240K resolution and a 50 milisecond maximum injection time, MS2 analysis was performed with HCD fragmentation in the ion trap with 32% normalized collision energy, 200-1200 m/z scan range, 18 milisecond maximum injection time, centroid format, and a rapid scan rate. Data was search against the human proteome database (canonical sequences downloaded from Uniprot 10/22/2020) using the default parameters in MaxQuant[33,34] (version 1.6.12.0), with the exception that match-between-runs was enabled (0.7 min time window) and a variable modification (361.14601 Da) representing the addition of biotin phenol to tyrosine residues was included.

Single cell RNA sequencing analysis

The presence or absence of CNVs in individual cells was assessed using CONICSmat (v1.0)[35]. Briefly, a two-component Gaussian mixture model was fit to the average expression values of genes on chromosome 22q across all cells assessed. CNVs were assessed in cells from tumor samples with copy-number loss of chromosome 22q at a bulk level as determined by DNA methylation, and for cells from copy-neutral normal dura samples. The command 'plotAll' from the CONICSmat R package was run with the parameters 'repetitions=100, postProb=0.75'. Cells with a posterior probability less than 0.15 were identified as tumor, while cells with a posterior probability greater than 0.85 were identified as normal. Clusters with greater than 80% of cells with intact chromosome 22q were determined to be non-meningioma cell clusters. The pericyte cluster contained an intermediate proportion of cells with or without loss of chromosome 22q, suggesting this cluster may represent both normal and tumor cells in the perivascular space. Standard immune, neural, and vascular markers in the top 50 differentially expressed genes of the non-meningioma cell clusters were used to classify non-tumor clusters. Cell cycle phases of individual cells were assigned with the standard 'CellCycleScoring' function in Seurat. Using single-cell cell cycle marker genes[36], average expression levels were calculated for each cell using G2M and S phase marker genes, respectively. If both average expression levels were less than 0, cells were classified as G1 phase. Otherwise, they were classified as either G2M or S phase, depending on which average expression was greater. Meningioma cell clusters were labeled based on cell cycle phases of cells and gene programs were identified by inspection of the top 50 differentially expressed genes. Gene ontology and pathway analyses with Enrichr and literature searches via Pubmed of differentially expressed genes helped identify upregulated pathways in meningioma cell clusters.

Reference transcriptomic signatures of single-cell clusters were generated using CIBERSORTx[37]. CIBERSORTx was run on a counts per million (CPM) matrix of all genes and 300 randomly sampled cells per cluster with a minimum expression fraction of 0.1 and default settings for all other parameters. Bulk RNA sequencing expression of meningiomas was deconvolved with CIBERSORTx using CPM expression of genes across bulk samples and with the generated single-cell transcriptomic signatures.

Magnetic resonance imaging analysis

All patients in the discovery cohort underwent preoperative magnetic resonance imaging (MRI) on clinical scanners at either 1.5 or 3.0 Tesla field strength. MRI protocols varied across the study period, but all patients included for image analysis (n=169) had T1 pre- and post-intravenous gadolinium contrast agent administration sequences, T2-weighted spin echo sequences, and T2-weighted fluid attenuated inversion recovery (FLAIR) sequences. Post-contrast T1 images evaluated in this study were high-resolution 3D, allowing for multiplanar reconstruction. Evaluation of meningioma proximity to dural venous sinuses was performed qualitatively by a board-certified radiologist with a Certificate of Added Qualification in Neuroradiology (J.E.V-M.) on post-contrast T1 images. Meningiomas were classified as involving a dural venous sinus if they abutted a dural reflection or invaded the sinus.

ChIP sequencing and enhancer/super-enhancer analysis

FASTQ reads were trimmed to remove low quality reads and adaptors with TrimGalore and uniquely mapped reads were aligned to the human reference genome hg19/GRCh37 with the Burrows-Wheeler Aligner[7]. SAMtools was used to sort and index BAMs, and PCR duplicates were removed with PicardTools. Peaks were called using MACS2 with the default log2 fold change enrichment of 2 compared to input and a p-value cutoff of 10^{-5}. Consensus peaksets and normalized H3K27ac densities were generating using the DiffBinds R package (Bioconductor v3.10). Peaks present in at least 2 tumor samples were used to generate a consensus peakset and overlapping peaks were merged. Peaks on chromosomes X or Y and peaks intersecting ENCODE blacklisted regions v1 on haplotype chromosomes were excluded from analysis. Bigwig tracks were generated using DeepTools (v3.1.2) with RPKM normalization and were visualized using Integrative Genomics Viewer

software. Super-enhancers were called using ROSE with default parameters[38,39]. Gene set enrichment networks were generated using ClueGO and visualized in Cytoscape[40,41]. Prediction of FOXM1-regulated genes was performed by first identifying FOXM1 binding motif sites using Homer to scan across the genome for the known FOXM1 motif. These sites were intersected with H3K27ac peaks in the consensus meningioma peakset, annotated to the nearest gene using Homer, and intersected with genes positively and significantly (FDR<0.05) correlated with FOXM1 expression as well as genes upregulated in the Hypermitotic meningiomas compared to tumors from other DNA methylation groups (FDR<0.05).

ChIP QPCR

ChIP qPCR was performed using the EZ-Magna ChIP A/G Chromatin Immunoprecipitation Kit (#17-10086, Millipore), according to manufacturer's instructions. Briefly, cells were fixed in 1% formaldehyde and sonicated to fragment sizes of 200-800 bp. Samples were incubated overnight with 10 µg USF1 antibody (#ab180717, Abcam) or IgG antibody bound to protein A and protein G magnetic beads. After antibody incubation, samples were washed once each with high salt, low salt, lithium chloride and TE buffers. Samples were de-crosslinked by incubation at 65°C for 4 hours, followed by incubation at 95°C for 10 minutes, and purified using a PCR purification kit (#K3100-01, Invitrogen). QPCR was performed using PowerUp SYBR Green Master Mix (#A25918, Thermo Fisher Scientific) (Supplementary table 14).

Patients

Patients were treated with Abemaciclib 100 mg *per os* twice daily. Treatment was held in the setting myelosuppression (absolute neutrophil count less than 1.5), and treatment-associated diarrhea was managed with over-the-counter medications. Meningioma volumes on serial magnetic resonance imaging studies were determined using MIM (MIM Software Inc), and the electronic medical record for all patients was reviewed in early 2021.

Nomograms

Prognostic models for LFFR were generated using multivariable Cox regression via the survival R package (v3.2-13). The proportional hazards assumption was confirmed by visual inspection of the Schoenfeld residuals and the Schoenfeld global test[42]. Variables included in the final model were selected by a two-step process, first by a univariable Cox regression threshold of $p \leq 0.05$, followed by selection of features with greatest variable importance as estimated by the Breiman permutation method using concordance as the model metric[43]. The top 7 features were selected to allow for at least 10 events per variable in the final model. This process was repeated for creation of the DNA methylation group model and the CNV group model. Models were compared using the bootstrapped time-dependent delta-AUC and delta-Brier-score for LFFR at 5 years[44]. The survAUC R package (v1.0-5) was used to calculate time-dependent AUC and Brier-scores. Nomograms based on the final Cox models were visualized using the 'nomogram' function of the rms R package (v6.2-0). Within nomograms, each variable contributes points (top row) to the total score, which estimates the probably of 5-year LFFR (bottom 2 rows)[45]. Cox model calibration of 5-year LFFR was estimated using the 'calibrate' function of the rms R package with default settings, utilizing Kaplan-Meier estimates, bootstrapping, and with an average group size of 50 subjects per calibration level. Unless otherwise specified, all bootstrap procedures were performed with 500 iterations. Recursive partitioning analysis of CNV and methylation groups was performed using the rpart R package (v4.1.16), with a minimum of 30 observations per split attempt and minimum of 15 observations per terminal leaf. The optimal complexity parameter was determined by 5-fold cross-validation, with selection of the most parsimonious model defined as the model with fewest splits and no more than one standard-error above the error of the best model[46]. Finally, interactive web nomogram graphical user interfaces were created using the DynNom R package (v5.1.0).

Supplementary references

1. Wilkerson, M. D. & Hayes, D. N. ConsensusClusterPlus: a class discovery tool with confidence assessments and item tracking. *Bioinformatics* **26**, 1572–1573 (2010).
2. Zhou, W., Triche, T. J., Laird, P. W. & Shen, H. SeSAMe: reducing artifactual detection of DNA methylation by Infinium BeadChips in genomic deletions. *Nucleic Acids Res* **46**, e123–e123 (2018).
3. Benelli, M., Romagnoli, D. & Demichelis, F. Tumor purity quantification by clonal DNA methylation signatures. *Bioinformatics* **34**, 1642–1649 (2018).
4. Vasudevan, H. N. *et al.* Comprehensive Molecular Profiling Identifies FOXM1 as a Key Transcription Factor for Meningioma Proliferation. *Cell Reports* **22**, 3672–3683 (2018).

5. Kline, C. N. *et al.* Targeted next-generation sequencing of pediatric neuro-oncology patients improves diagnosis, identifies pathogenic germline mutations, and directs targeted therapy. *Neuro Oncol* **19**, 699–709 (2017).
6. Magill, S. T. *et al.* Multiplatform genomic profiling and magnetic resonance imaging identify mechanisms underlying intratumor heterogeneity in meningioma. *Nature Communications* **11**, 4803 (2020).
7. Li, H. & Durbin, R. Fast and accurate short read alignment with Burrows-Wheeler transform. *Bioinformatics* **25**, 1754–1760 (2009).
8. DePristo, M. A. *et al.* A framework for variation discovery and genotyping using next-generation DNA sequencing data. *Nat Genet* **43**, 491–498 (2011).
9. McKenna, A. *et al.* The Genome Analysis Toolkit: a MapReduce framework for analyzing next-generation DNA sequencing data. *Genome Res* **20**, 1297–1303 (2010).
10. Talevich, E., Shain, A. H., Botton, T. & Bastian, B. C. CNVkit: Genome-Wide Copy Number Detection and Visualization from Targeted DNA Sequencing. *PLoS Comput Biol* **12**, e1004873 (2016).
11. Love, M. I., Huber, W. & Anders, S. Moderated estimation of fold change and dispersion for RNA-seq data with DESeq2. *Genome Biology* **15**, 550 (2014).
12. Zhu, A., Ibrahim, J. G. & Love, M. I. Heavy-tailed prior distributions for sequence count data: removing the noise and preserving large differences. *Bioinformatics* **35**, 2084–2092 (2019).
13. Chen, E. Y. *et al.* Enrichr: interactive and collaborative HTML5 gene list enrichment analysis tool. *BMC Bioinformatics* **14**, 128 (2013).
14. Kuleshov, M. V. *et al.* Enrichr: a comprehensive gene set enrichment analysis web server 2016 update. *Nucleic Acids Res.* **44**, W90-97 (2016).
15. Aran, D., Hu, Z. & Butte, A. J. xCell: digitally portraying the tissue cellular heterogeneity landscape. *Genome Biology* **18**, 220 (2017).
16. Rouillard, A. D. *et al.* The harmonizome: a collection of processed datasets gathered to serve and mine knowledge about genes and proteins. *Database (Oxford)* **2016**, (2016).
17. Andrews, S. *FastQC*.
18. Langmead, B. & Salzberg, S. L. Fast gapped-read alignment with Bowtie 2. *Nat Methods* **9**, 357–359 (2012).
19. Auwera, G. A. V. der *et al.* From FastQ Data to High-Confidence Variant Calls: The Genome Analysis Toolkit Best Practices Pipeline. *Current Protocols in Bioinformatics* **43**, 11.10.1-11.10.33 (2013).
20. Cingolani, P. *et al.* A program for annotating and predicting the effects of single nucleotide polymorphisms, SnpEff: SNPs in the genome of Drosophila melanogaster strain w1118; iso-2; iso-3. *Fly (Austin)* **6**, 80–92 (2012).
21. Cingolani, P. *et al.* Using Drosophila melanogaster as a Model for Genotoxic Chemical Mutational Studies with a New Program, SnpSift. *Front Genet* **3**, 35 (2012).
22. Findakly, S. *et al.* Meningioma cells express primary cilia but do not transduce ciliary Hedgehog signals. *Acta Neuropathologica Communications* **8**, 114 (2020).
23. Clark, V. E. *et al.* Genomic analysis of non-NF2 meningiomas reveals mutations in TRAF7, KLF4, AKT1, and SMO. *Science* **339**, 1077–1080 (2013).
24. Sahm, F. *et al.* DNA methylation-based classification and grading system for meningioma: a multicentre, retrospective analysis. *The Lancet Oncology* **18**, 682–694 (2017).
25. Youngblood, M. W. *et al.* Correlations between genomic subgroup and clinical features in a cohort of more than 3000 meningiomas. *Journal of Neurosurgery* **1**, 1–10 (2019).
26. Paramasivam, N. *et al.* Mutational patterns and regulatory networks in epigenetic subgroups of meningioma. *Acta Neuropathol* **138**, 295–308 (2019).
27. Prager, B. C. *et al.* The Meningioma Enhancer Landscape Delineates Novel Subgroups and Drives Druggable Dependencies. *Cancer Discov* (2020) doi:10.1158/2159-8290.CD-20-0160.
28. Shukla, S. A. *et al.* Comprehensive analysis of cancer-associated somatic mutations in class I HLA genes. *Nat Biotechnol* **33**, 1152–1158 (2015).
29. Cao, H. *et al.* An integrated tool to study MHC region: accurate SNV detection and HLA genes typing in human MHC region using targeted high-throughput sequencing. *PLoS One* **8**, e69388 (2013).
30. Wang, K., Li, M. & Hakonarson, H. ANNOVAR: functional annotation of genetic variants from high-throughput sequencing data. *Nucleic Acids Res* **38**, e164 (2010).
31. Jurtz, V. *et al.* NetMHCpan-4.0: Improved Peptide-MHC Class I Interaction Predictions Integrating Eluted Ligand and Peptide Binding Affinity Data. *J Immunol* **199**, 3360–3368 (2017).
32. Łuksza, M. *et al.* A neoantigen fitness model predicts tumour response to checkpoint blockade immunotherapy. *Nature* **551**, 517–520 (2017).

33. Cox, J. & Mann, M. MaxQuant enables high peptide identification rates, individualized p.p.b.-range mass accuracies and proteome-wide protein quantification. *Nat Biotechnol* **26**, 1367–1372 (2008).
34. Prianichnikov, N. *et al.* MaxQuant Software for Ion Mobility Enhanced Shotgun Proteomics. *Mol Cell Proteomics* **19**, 1058–1069 (2020).
35. Müller, S., Cho, A., Liu, S. J., Lim, D. A. & Diaz, A. CONICS integrates scRNA-seq with DNA sequencing to map gene expression to tumor sub-clones. *Bioinformatics* **34**, 3217–3219 (2018).
36. Tirosh, I. *et al.* Dissecting the multicellular ecosystem of metastatic melanoma by single-cell RNA-seq. *Science* **352**, 189–196 (2016).
37. Newman, A. M. *et al.* Determining cell type abundance and expression from bulk tissues with digital cytometry. *Nature Biotechnology* **37**, 773–782 (2019).
38. Whyte, W. A. *et al.* Master Transcription Factors and Mediator Establish Super-Enhancers at Key Cell Identity Genes. *Cell* **153**, 307–319 (2013).
39. Lovén, J. *et al.* Selective Inhibition of Tumor Oncogenes by Disruption of Super-Enhancers. *Cell* **153**, 320–334 (2013).
40. Bindea, G. *et al.* ClueGO: a Cytoscape plug-in to decipher functionally grouped gene ontology and pathway annotation networks. *Bioinformatics* **25**, 1091–1093 (2009).
41. Shannon, P. *et al.* Cytoscape: A Software Environment for Integrated Models of Biomolecular Interaction Networks. *Genome Res* **13**, 2498–2504 (2003).
42. Schoenfeld, D. Partial residuals for the proportional hazards regression model. *Biometrika* **69**, 239–241 (1982).
43. Breiman, L. Random Forests. *Machine Learning* **45**, 5–32 (2001).
44. Song, X. & Zhou, X.-H. A SEMIPARAMETRIC APPROACH FOR THE COVARIATE SPECIFIC ROC CURVE WITH SURVIVAL OUTCOME. *Statistica Sinica* **18**, 947–965 (2008).
45. Iasonos, A., Schrag, D., Raj, G. V. & Panageas, K. S. How to build and interpret a nomogram for cancer prognosis. *J Clin Oncol* **26**, 1364–1370 (2008).
46. Hastie, T., Tibshirani, R. & Friedman, J. *The Elements of Statistical Learning: Data Mining, Inference, and Prediction*. (2009).